Pol. J. Environ. Stud. Vol. XX, No. X (XXXX), 1-22
DOI: *10.15244/pjoes/210106* ONLINE PUBLICATION DATE: 2025-12-01

Original Research

DEM and CFD Modeling of Pore-Scale Hydraulic Performance of Loose Gravel Soil from a Large Reservoir Area under Planning in the Upper Yellow River, China

Zhijun Wang[1, 2, 3]*, Qibin Fu[1], Yajie Zhou[1]

[1]College of Energy and Power Engineering, Lanzhou University of Technology, Lanzhou 730050, China
[2]Smart Agriculture Irrigation Equipment Key Laboratory, Ministry of Agriculture and Rural Affairs, Lanzhou, 730050, Gansu, China
[3]Baiyin Research Institute of Novel Materials of LUT, Baiyin 730900, China

Received: 19 April 2025
Accepted: 31 August 2025

Abstract

The failure mechanism of internal seepage flow in geotechnical bank slopes is complex. Investigating the microscale characteristics of pore structure and seepage flow behavior forms the scientific foundation for preventing slope collapse. This study focuses on Loose Gravel Soil from the Heishanxia reservoir area of the Yellow River. Multi-view stereo modeling technology is employed to scan and reconstruct coarse aggregate particles above d_{10} (0.14 mm), d_{20} (0.20 mm), and d_{30} (0.28 mm) from the gradation curve into clumps through multi-angle photogrammetric reconstruction, while finer particles below these thresholds are modeled as spherical grains. Three virtual samples (B-10, B-20, B-30) with varying proportions of spherical particles were developed in PFC 5.0 using pre-compaction methods. The rationality of the modeling approach is verified by comparing the calculated permeability with experimentally measured values. To further validate the methodological efficacy, a variable hydraulic gradient soil column experiment replicating reservoir operational conditions was implemented, followed by a comparative analysis of seepage characteristics through Stokes flow solver simulations. Following the selection of representative elementary volumes (REV) using nine-point sampling, quantitative analyses of pore-space topology, including coordination number, pore size, pore morphology, and fractal dimension, are conducted. Three-dimensional single-phase flow simulations are performed along the X/Y/Z directions using pore network modeling (PNM), and the seepage characteristics were analyzed. The proposed modeling methodology establishes a foundational

*e-mail: wzj1159@163.com
Tel.: +86-189-9319-0809
°ORCID iD: 0000-0003-1197-2318

framework for the future prevention and control of seepage flow-induced instability in the Yellow River Stone Forest sandy conglomerate bank slopes.

Keywords: loose gravel soil, DEM-CFD, pore structure, three-dimensional reconstruction, seepage flow characteristics

Introduction

Seepage flow erosion within geotechnical materials frequently leads to ecological and environmental challenges, such as soil erosion, and constitutes a primary cause of various engineering issues, including reservoir dam failures, uneven foundation settlement, and slope instability [1]. Therefore, a comprehensive investigation into the microscopic characteristics of seepage flow erosion has become a critical focus in both academic research and engineering practice [2-4]. In China, for example, recurrent seepage flow-induced collapses of soil-rock mixture slopes in the Three Gorges Reservoir area along the Yangtze River pose threats to the reservoir's operational safety and negatively impact the sustainable development of the surrounding ecosystem [5-7]. As the cradle of Chinese civilization, the Yellow River faces considerable challenges in the Ningxia-Inner Mongolia reach, including ice flood prevention, flood control, and sediment management. Therefore, the Chinese government has proposed constructing the Dalioushu High Dam at the outlet of the Heishanxia Gorge. This dam, along with the Longyangxia and Liujiaxia reservoirs, is intended to optimize water resource distribution across the basin following the implementation of the South-to-North Water Diversion Project (Fig. 1a)). Within the proposed reservoir area, the Loose Gravel Soil bank slopes of the Yellow River Stone Forest, shaped by long-term geological tectonic activity and wind-water erosion, often display weathered and semi-weathered surface layers. Their loose granular structure results in pores characterized by multi-scale, multi-phase, and non-uniform properties [8], making them especially susceptible to instability and collapse after the construction and impoundment of the Heishanxia hydropower project. Given the complex mechanisms underlying internal seepage flow failure, a detailed analysis of pore structure characteristics and seepage flow behavior at the microscopic scale is essential for formulating effective strategies to prevent and mitigate slope instability.

In the field of microscopic pore research in geotechnical materials, the three-dimensional reconstruction and analysis of pore structures have evolved significantly, progressing from traditional to advanced methods. Initial studies predominantly utilized techniques such as focused ion beam (FIB) [9] and scanning electron microscopy (SEM) [10, 11] to acquire three-dimensional pore images. Although these methods provide visual information on pore structures, they are often constrained by resolution and imaging depth, making it difficult to fully capture the complex internal pore structures and connectivity of porous media. With the development of technologies such as X-ray tomography (XRT) [12] and computed tomography (CT) [13], three-dimensional pore reconstruction has made substantial progress. X-CT imaging has emerged as one of the most effective techniques for acquiring three-dimensional images of pore spaces in porous media [14-16]. Methods for reconstructing the microstructure of two-phase and multi-phase porous media based on digital image information and statistical analysis have gained broad application. Although nondestructive testing techniques such as X-CT can accurately restore the micro-pore structures of rock and soil masses, they still face challenges such as high equipment costs and limitations on sample size and quantity [17], which hinders comprehensive characterization of pore structure features in large-scale geotechnical materials.

With recent advancements in computational science and image processing technologies, many researchers have increasingly explored the characterization and analysis of pore structures using numerical simulations [18-20], optimized reconstruction algorithms [21], and neural network algorithms [22-24]. Among these approaches, the Discrete Element Method (DEM) [25, 26] has received considerable attention due to its convenience, repeatability, visualization capabilities, and effectiveness in depicting microscopic pore structures for seepage flow analysis. For instance, Zhang et al. [27] applied spherical three-dimensional modeling and numerical evaluation methods to optimize the anti-clogging performance of permeable pavement structures. However, because spherical modeling cannot accurately represent actual aggregate shapes, it can result in inaccuracies in characterizing the model's permeability and hydraulic performance. Therefore, Zhang et al. [28] utilized photogrammetric analysis technology to accurately model coarse aggregates in open-graded asphalt, combining DEM with Computational Fluid Dynamics (CFD) to investigate the hydraulic behavior of two-dimensional asphalt cross-sections. Pieralisi et al. [29] combined DEM and CFD methods to evaluate changes in the permeability of pervious concrete by modifying its composition and compaction process. Although these studies considered the influence of DEM aggregate particle shapes on model permeability, most investigations into seepage flow patterns are based on two-dimensional cross-sectional analyses, with limited research on three-dimensional microscopic pore-scale seepage flow characteristics.

Three-dimensional spatial models in the numerical simulation of fluid flow through porous media provide a more comprehensive representation of seepage flow

behavior in geotechnical materials, effectively capturing changes in seepage flow paths and velocity distributions in practical engineering applications, particularly in projects such as reservoirs, dams, slopes, and foundation pits [30, 31]. When analyzing three-dimensional pore structure characteristics at the microscopic scale, selecting an appropriate representative elementary volume (REV) to balance model size and computational requirements is essential. Koestel et al. [32] determined the REV of soil pore structures through quantitative analysis of porosity, pore size, and permeability, establishing criteria for REV selection. Based on Koestel's research, Cai et al. [33] integrated the pore network model (PNM) method with REV, using Avizo software to investigate the permeability of pervious concrete. For fluid flow problems, many previous studies have employed methods such as the lattice Boltzmann method (LBM) and Level Set [34, 35]. Although these methods can accurately simulate pore-scale flow at the mesoscopic scale, they require substantial memory and computational resources for high-resolution models and complex pore geometries. In contrast, the PNM method simplifies fluid flow simulation in porous media [36], reducing computational demands while maintaining accuracy and effectively representing spatial structural features such as pore size, connectivity, and coordination number in three dimensions.

Based on these considerations, this study focuses on the Loose Gravel Soil of the slope in the Yellow River Stone Forest reservoir area within the Heishanxia section. The objective is to establish a three-dimensional reconstruction model of the pore structure to investigate seepage flow characteristics at the microscopic scale. The real aggregate particles are constructed into clump models through multi-view stereoscopic real modeling, and combined with spherical fine particles, a virtual sample of Loose Gravel Soil is constructed by the preloading method according to the gradation. A representative elementary volume (REV) was selected to quantitatively characterize the topological structure of the pore space, and the model's validity was verified by comparing the computed permeability with experimentally measured values. Seepage flow characteristics were further simulated based on the PNM. In addition, a variable hydraulic gradient soil column seepage flow experiment was designed to simulate reservoir operations, and the results were compared to Stokes solver analyses to validate the modeling approach. This study aims to establish a methodological foundation for future prevention and mitigation of seepage flow-induced instability in the slopes of the Yellow River Stone Forest Loose Gravel Soil. The proposed three-dimensional pore structure reconstruction method is also expected to be applicable in analyzing the processes and mechanisms of soil erosion caused by internal seepage flow in geotechnical materials.

Materials and Methods

Sample Preparation

The Yellow River Stone Forest is located upstream of the Heishanxia section along the Yellow River mainstem. Upon completion of the downstream Daliushu High Dam, areas below the 1380 m elevation within the Stone Forest section will be inundated, forming part of the reservoir (Fig. 1b)). The slopes are extensively covered with Loose Gravel Soil (Fig. 1c)), primarily consisting of subangular gravels, sand particles, and clayey silts with well-developed pore structures. Post-impoundment seepage flow pressures can trigger engineering hazards such as bank instability and slope failures. This study targets this region, collecting Loose Gravel Soil samples from five locations within the inundation zone shown in Fig. 1b).

The gravelly sandstone soil displays a loosely compacted granular structure. Prior to sampling, surface aeolian deposits were carefully removed. Undisturbed soil specimens were extracted at a depth of 10 cm using a ring cutter. The specimens were used for porosity and natural density measurements. Then, bulk samples were collected from the corresponding strata for experimental characterization and numerical modeling. The constant-head permeability test was systematically conducted on sandy gravel soils, and the measured hydraulic conductivity values were compared to numerical simulation results to validate the model. The fundamental geotechnical properties of the specimens, determined in accordance with Chinese National Standards GB/T 14684-2022 (Test methods for building sand) and GB/T 34533-2023 (Technical specification for soil tests), are summarized in Table 1.

Particle size distribution analysis was conducted using the sieving method. Previous studies [37, 38] indicate that boundary effects can be avoided when the specimen diameter exceeds five times the maximum particle size. Due to constraints of the experimental apparatus (5-10 cm diameter), scaled specimens were prepared using the equivalent substitution method [39, 40], whereby particles coarser than 10 mm were removed. The resulting gradation curve (Fig. 2) yields a uniformity coefficient C_u = 15.3 and a curvature coefficient C_c = 0.73. This indicates that the overall gradation of the gravelly sandstone crushed stone soil sample is good, with a wide distribution of various grain groups. However, the soil contains a higher proportion of fine particles, and the size variation among these fine particles is relatively small.

Geometric Modeling

The sandy conglomerate gravel soil exhibits a loose structure. For simulations, the discrete element method (DEM) more accurately represents the structural and positional relationships among actual particles, enabling detailed investigation of the pore structure. This study

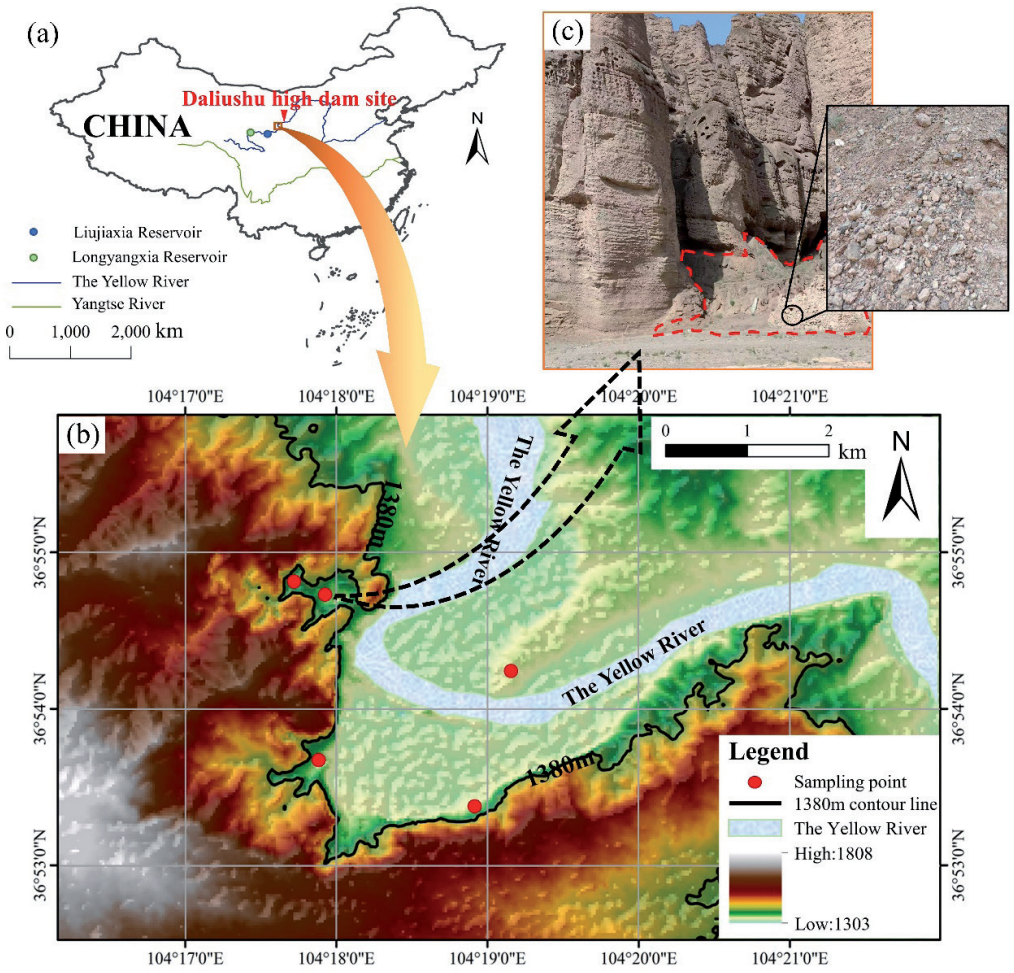

Fig. 1. The study area and sampling points. a) location; b) landform of the study area; c) sampling area, where the red dotted line is the Loose Gravel Soil.

Table 1. Basic physical parameters of Loose Gravel Soil.

Number	Density (kg/m^3)	Porosity (%)	Permeability (10^{-11} m^2)	Moisture Content (%)	C_u	C_c
Loose Gravel Soil	1.86	32.7	0.314	0.81	15.3	0.73

utilized PFC 5.0 (Itasca Consulting Group; http://www.itascacg.com) to model the particles of sandy conglomerate gravel soil. Following the methodology outlined in the literature [28], the red segment of the continuous gradation range in Fig. 2, after excluding the particle sizes at both ends of the distribution (DEM-CFD), is selected as the modeling basis. The particle diameters smaller than d_{10} (0.14 mm), d_{20} (0.20 mm), and d_{30} (0.28 mm) within this range are generalized as spherical particles, while the larger particles are modeled using aggregate photography techniques. The models containing different proportions of spherical particles are labeled as B-10, B-20, and B-30, respectively.

Fig. 3. The aggregate imaging protocol involved suspending Loose Gravel Soil samples from the Yellow River Stone Forest area using transparent filaments connected to a low-power adjustable motor. Controlled rotational motion facilitated systematic photographic acquisition across multiple elevation planes for analytical processing [28].

In 3DF Zephyr (3DFLOW; http://www.3dflow.net), multi-view stereo matching technology is applied to analyze the photographs captured from different angles. Identical feature points in the images are identified and matched to calculate their positions in three-dimensional space. The depth value of each pixel, representing the distance between each pixel and the imaging device, is determined through stereo matching. Combined with the focal length and optical center coordinates, the corresponding three-dimensional coordinates are derived using Equations (1) and (2). This set of coordinates forms a sparse point cloud.

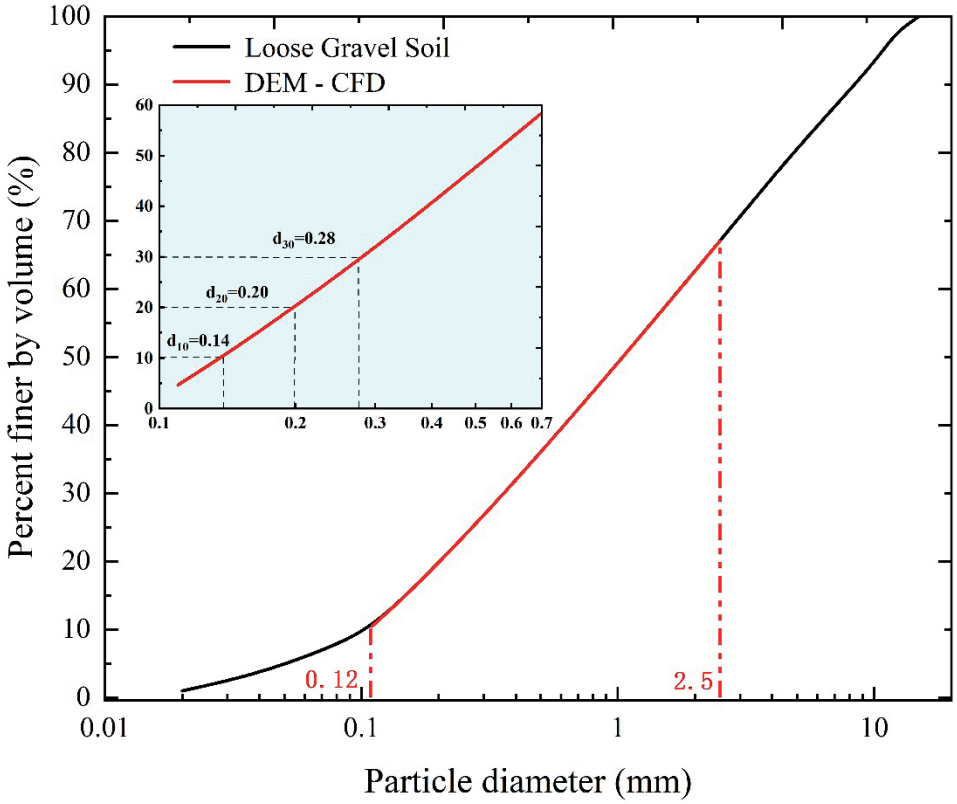

Fig. 2. Grading distribution of Loose Gravel Soil.

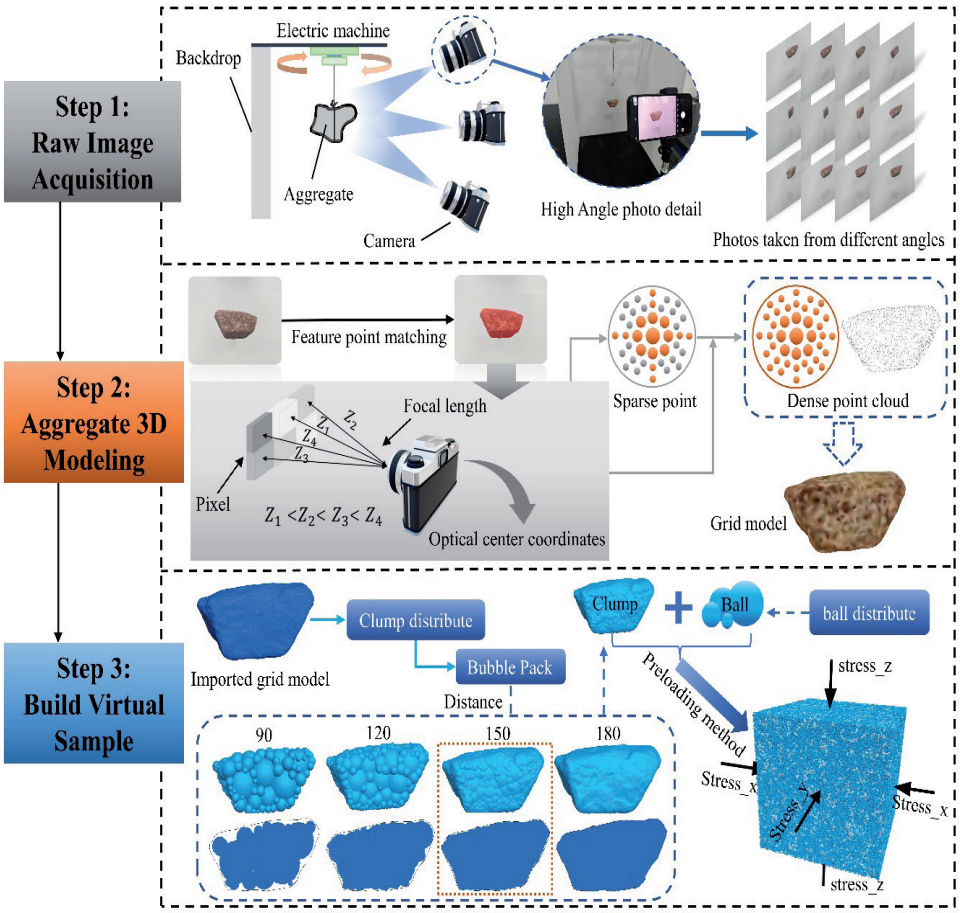

Fig. 3. Geometric modeling process.

$$X = \frac{(x - c_x) \cdot Z}{f_x} \tag{1}$$

$$Y = \frac{(y - c_y) \cdot Z}{f_y} \tag{2}$$

where Z is the depth value; f_x and f_y are the focal lengths of the imaging device; c_x and c_y are the coordinates of the optical center.

Cloth Simulation Filter (CSF) [41] algorithm optimization enhanced point cloud fidelity by outlier removal and noise reduction. Feature points with close depth values can be converted into three-dimensional coordinates to construct a dense point cloud, followed by Poisson surface reconstruction generating watertight mesh models.

The import of 72 clump templates into PFC 5.0 required internal vectorization via the Bubble Pack algorithm [42], with surface topography regulated through sphere centroid spacing adjustments using the "distance" command [43]. Virtual specimen generation replicated actual gradation profiles, with spherical fines occupying interstitial voids between realistic aggregates. Initial particle overlaps were removed through servo-controlled pre-compaction [44], resulting in a target porosity of 30% in the final virtual specimens. Due to the high porosity exhibited by the Loose Gravel Soil sample, variations in aggregate and pore structures are not highly sensitive as long as the total porosity of the model remains comparable [28]. Under these conditions, the virtual specimen is constructed as a cube with a 2 cm edge length.

Since the model relies only on mechanical contact among particles and between particles and boundaries, the mechanical properties of the system have not been evaluated. Mechanical interactions were modeled exclusively using linear contact formulations (Equation (3)) [45, 46].

$$F_n = K_n \cdot R_n \tag{3}$$

where F_n is the normal contact force, K_n is the normal contact stiffness coefficient, and R_n is the normal overlap amount. The calculation of shear force and tangential overlap is shown in Equation (4).

$$\Delta F_s = -K_s \cdot \Delta R_s \tag{4}$$

where ΔF_s is the shear force; K_s is the tangential contact stiffness coefficient; ΔR_s is the tangential overlap amount.

Pore Structure 3D Reconstruction

Direct export of the three-dimensional model data of virtual specimens from PFC 5.0 can result in excessive memory consumption. A sequential sectioning method [47] was applied to the B-30, B-20, and B-10 virtual specimens to mitigate this. Model slices were generated along the Z-axis at 0.016 mm intervals. After trimming the edges, 1250 high-resolution slices (1250×1250 pixels) were processed to reconstruct the 3D pore architecture using digital image analysis.

The AVIZO platform (FEI Visualization Sciences Group; https://www.fei.com/software/amira-avizo)

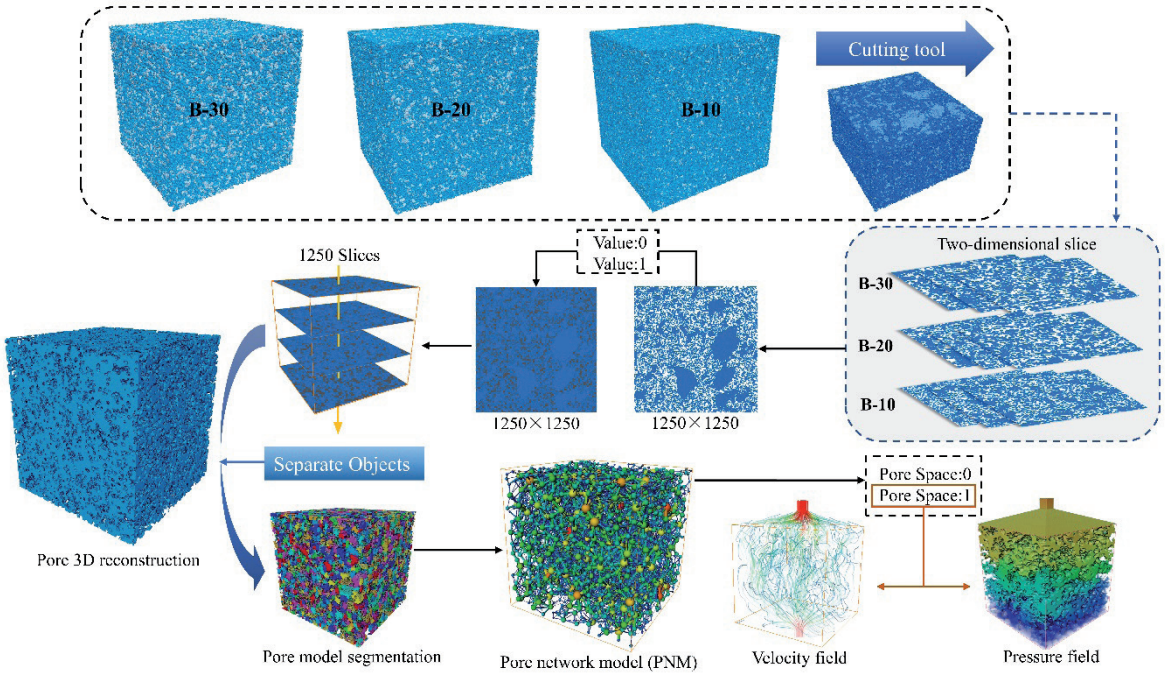

Fig. 4. Pore 3D reconstruction process.

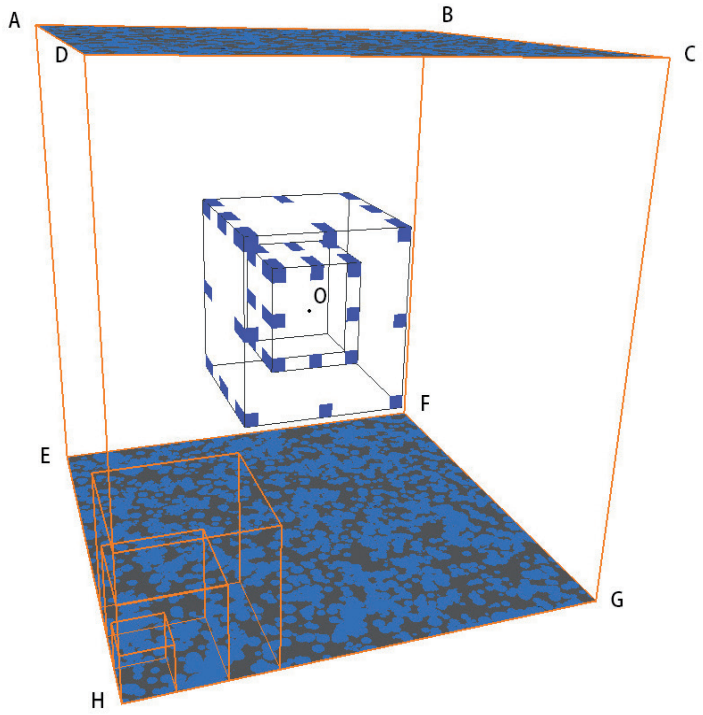

Fig. 5. REV extraction schematic.

performed threshold segmentation using Otsu's method to determine pore-grain interfaces. Interpolated slices were then stacked to reconstruct the 3D geometry. The Separate Objects module was employed to isolate regions with inadequate resolution or ambiguous segmentation. This preprocessing step ensured precision in the PNM construction and in subsequent fluid flow simulations through pores and throats, as illustrated in Fig. 4.

REV Extraction

The Representative Elementary Volume (REV) is defined as the minimum volumetric unit that statistically captures the microstructural characteristics of porous media when analyzing their macroscopic physical properties [32]. Conventional 2×2×2 mm^3 models used in pore-scale seepage flow simulations are inadequate for specimens containing heterogeneously distributed pores >2 mm [48-50]. This necessitates careful REV selection to balance physical representativeness and computational feasibility. The B-10 specimen serves as the primary case for subsequent REV determination.

REV determination for geomaterials requires consideration of both geometric configuration and spatial anisotropy of pore structures. Following established methodologies, a nine-point sampling scheme (Fig. 5) is implemented to characterize virtual pore structures [32, 51, 52]. The protocol sequentially selects eight vertices (A–H) and the centroid (O) of the cubic structure. Starting with reference points (H and O), spatial increments (L, 2L, ...) expand sub-cube dimensions until encompassing the entire structure, generating multiple scaled sub-volumes per reference point. A total of 180 sub-cubes are created for comprehensive parameter correlation analysis.

Following Chu et al.'s [53] approximation criterion, maximum pore diameter emerges as the critical parameter for porosity-based REV determination, governing key transport properties, including permeability and thermal/electrical conductivity. Therefore, the REV dimension analysis focuses on porosity characterization.

Porosity-size relationships derived from nine-point sampled sub-cubes (Fig. 6) indicate optimal REV edge lengths of 400-600 voxels for the 3D pore architecture. Quantitative REV determination is achieved through porosity coefficient of variation (C_V) analysis (Fig. 7), eliminating subjective interpretation. Adopting Min's [54] 5% C_V threshold, 540 voxels (8.64×8.64×8.64 mm^3) is established as the optimal REV dimension for the 3D Loose Gravel Soil pore model.

Seepage Flow Simulation

PNM Single-Phase Flow Calculation

The computation of microscopic pore flow in porous media correlates with intra-pore flow dynamics. This study conducts pore-scale flow simulations using the XLabSuite Extension module integrated in Avizo. The fluid flows from high-pressure regions to low-pressure regions, where the pressure gradient demonstrates a linear correlation with flow quantity, as illustrated in Fig. 8. The flow rate q_{ij} between pores i and j is determined by Equation (5).

$$q_{ij} = g_{ij}(P_i - P_j) \tag{5}$$

where g_{ij} is the hydraulic conductivity of the throat between pore i and pore j, calculated from Equation (6); $P_i - P_j$ is the pressure difference between the two pores.

$$g_{ij} = \frac{\pi}{8\mu}\frac{r_{ij}^4}{l_{ij}} \tag{6}$$

$$Q = \sum(P_i - P_j)g_{ij} \tag{7}$$

where μ is the dynamic viscosity of the fluid; r is the throat radius; l is the throat length. The total flow rate Q can be calculated, as shown in Equation (7), by summing the flow rates of all interconnected pores.

The pore spaces in macropore-containing network models can be resolved by establishing linear equation systems through Equations (5) and (7). Permeability,

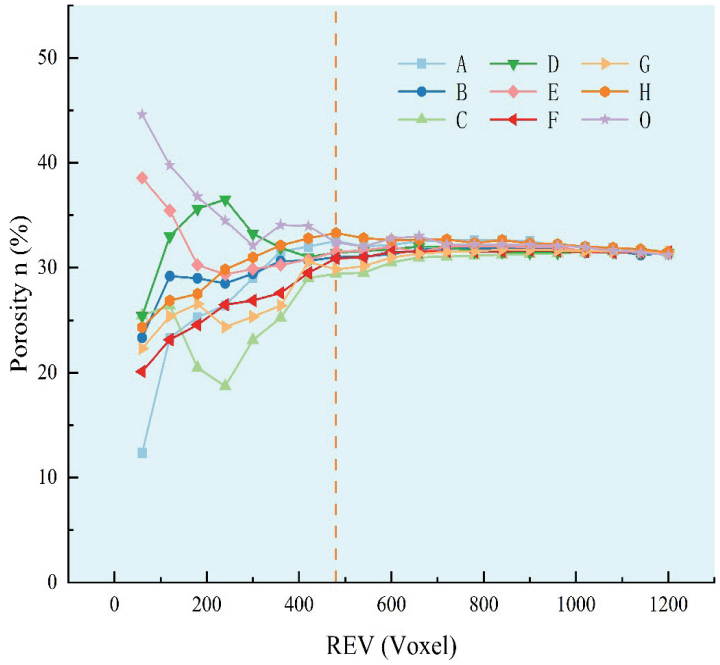

Fig. 6. Variations in the relationship between porosity and REV scale for Loose Gravel Soil.

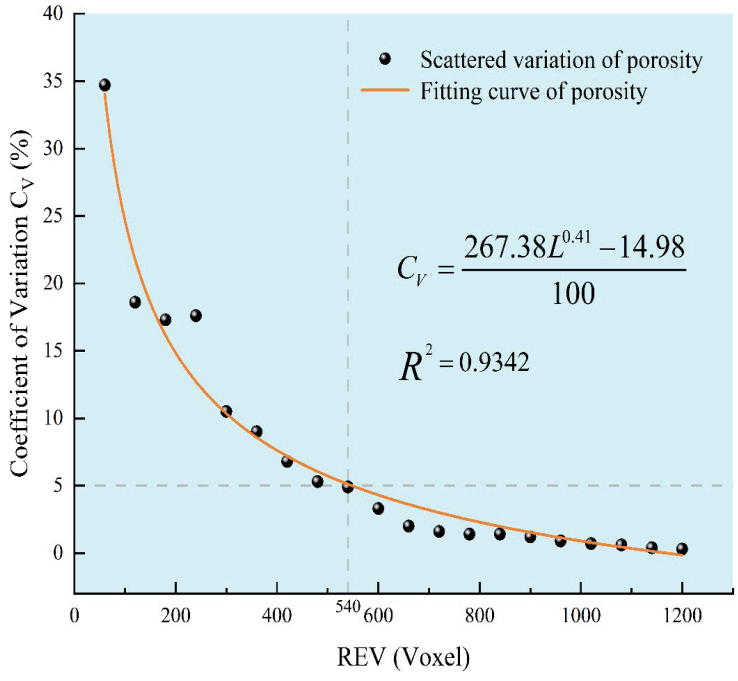

Fig. 7. Porosity coefficient of variation versus subsample size for Loose Gravel Soil.

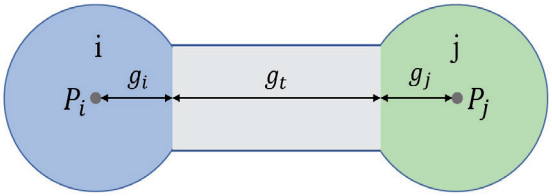

Fig. 8. Pore and throat connection unit model.

which quantifies the fluid transmission capacity of soil pores, is typically computed via Darcy's law.

$$K = \frac{Q\mu L}{\Delta P A} \tag{8}$$

In accordance with Darcy's law, Equation (8) enables the determination of the permeability of the virtual specimen REV. The accuracy of the model is verified by comparing it to experimental permeability measurements. In this context, ΔP represents the imposed pressure gradient at the boundaries; A is the cross-sectional area; L is the characteristic flow length.

Boundary condition initialization: Slip phenomena at fluid-solid interfaces are neglected, as they rarely occur in pore structures. The watertight geometric model establishes inlet and outlet pressures along the seepage flow direction, ensuring a quasi-static pore pressure distribution and facilitating fluid migration through pore networks. With fluid properties maintained at 20°C and a dynamic viscosity of 0.001 Pa·s, the boundary pressures are specified as 0.15 kPa (inlet) and 0 kPa (outlet).

Navier-Stokes Flow Calculation

In pore-scale seepage flow scenarios, the fluid exhibits a low flow velocity and minimal Reynolds numbers, justifying the omission of inertial forces. The Creeping Flow interface in COMSOL (COMSOL Inc.; http://www.comsol.com) applies the reduced Navier-Stokes equations to characterize mass-momentum dynamics in fluid motion, corresponding to Stokes flow [55]. The mathematical formulation of Stokes flow is presented in Equation (9).

$$\underbrace{\rho\left(\frac{\partial u}{\partial t} + u \cdot Vu\right)}_{1} = \underbrace{-\nabla p}_{2} + \underbrace{\nabla \cdot \left(\mu(\nabla u + (\nabla u)^T) - \frac{2}{3}\mu(\nabla u)I\right)}_{3} + \underbrace{F}_{4} \tag{9}$$

where u is fluid velocity; p is fluid pressure; ρ is fluid density; ∇ is the Laplace operator; μ is fluid dynamic viscosity; I is the identity matrix. The terms 1, 2, 3, and 4 correspond to inertial forces, pressure, viscous forces, and external forces acting on the fluid, respectively.

Defined as the ratio of inertial forces 1 to viscous forces 3, the Reynolds number remains exceptionally small in pore-scale flows, indicating laminar flow regimes and quasi-incompressible behavior within microscopic pores. The divergence-free constraint for incompressible fluids is expressed in Equation (10).

$$\nabla \cdot u = 0 \tag{10}$$

$$0 = -\nabla p + \nabla \cdot (\mu(\nabla u + (\nabla u)^T) \tag{11}$$

At ultralow Reynolds numbers, inertial forces become negligible in comparison to viscous forces 3, permitting their exclusion from computational models. In the absence of external forces (external force 4 = 0) and by substituting Equation (10), the reduced form of the Stokes equations is obtained as Equation (11). When the Reynolds number is extremely small, inertial forces are negligible relative to viscous forces and can be omitted from the calculations. In addition, as no external force is applied, the force acting on the fluid is zero. Substituting Equation (10) into the governing equation yields Equation (11), the simplified Stokes equation.

Based on the temporal evolution of the hydraulic gradient during reservoir impoundment, the erosion model validation framework established by Zhang et al. [56, 57] is implemented to examine depth-dependent flow velocity responses to hydraulic gradient variations in Loose Gravel Soil.

The test was conducted using the apparatus illustrated in Fig. 9. The soil column had a height of 20 cm, with piezometers BWK-1, BWK-2, and BWK-3 installed at depths of 15 cm, 10 cm, and 5 cm from the base, respectively. The upper end of the column was submerged to maintain a constant hydraulic head. Pore water pressure measurements were recorded at 30-second intervals, while the hydraulic gradient was incremented by 0.4 every 5 minutes through controlled adjustments of the free surface level in the water tank. Electrical signals acquired by the piezometers were processed via a data logger and transmitted to a computational unit to record temporal pressure variations at each monitoring point. Seepage flow velocities at each cross-section were subsequently calculated using Equation (12).

$$q = -k\frac{dp}{dx} \tag{12}$$

where q is the water flow velocity; k is the permeability measured in the experiment; dp is the pore water pressure; dx is the height of the permeable soil column.

In Stokes flow simulations, initial inlet and outlet boundary pressures were defined using pore water pressures measured per minute at each piezometer depth, with the outlet configured as a free surface. Since pore water pressure dynamically varied with hydraulic gradient changes during the test, the inlet pressure in Stokes flow calculations was proportionally adjusted to match hydraulic gradient variations. Quantitative comparison between seepage test results and Stokes flow simulation outcomes further validated the model's accuracy.

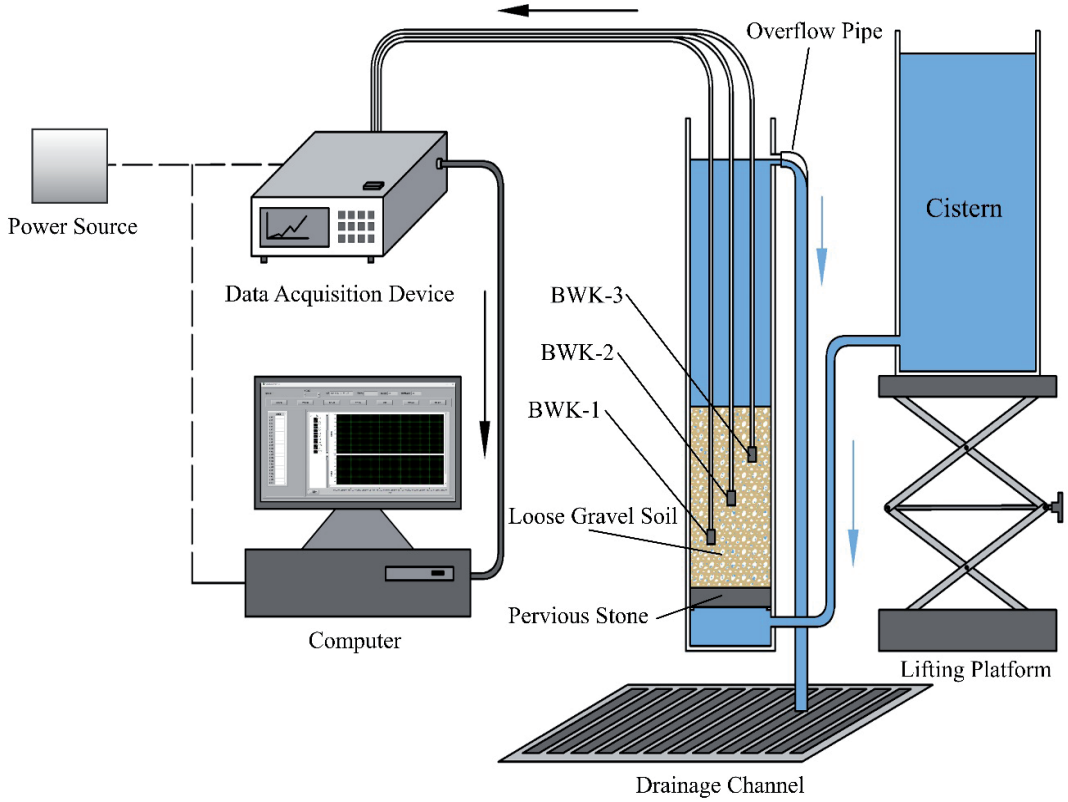

Fig. 9. Test apparatus for seepage.

Results

Verification of the Numerical Model

Permeability Analysis

Permeability is a key parameter in characterizing flow behavior in porous media. A comparative analysis between experimentally measured permeability values of soil specimens and model-calculated results allows for the validation of modeling accuracy [33]. This study utilizes the XLabSuite Extension module in AVIZO for permeability computations within the PNM.

The maximum permeability errors across spatial REV positions in B-10, B-20, and B-30 models were calculated as 8.6%, 15.1%, and 27.7% respectively. Extensive literature establishes that permissible errors for model-validated permeability remain within 30% [58-60]. All errors in our models satisfy this criterion, which confirms the robustness of the proposed modeling methodology and demonstrates its sufficient reliability for seepage flow simulations. These findings affirm the robustness of the proposed modeling approach for fluid flow simulations. In addition, permeability estimation errors show a gradual reduction as the percentage of spherical particles decreases. This correlation is attributed to variations in spherical particle fractions, which induce corresponding changes in pore structure complexity, enhancing the agreement between numerical permeability predictions and experimental results. Taking the B-10 model's REV-simulated Z-axis permeability versus experimental data (Table 2) as an example, permeability values display minimal spatial variation while maintaining a consistent pattern of slightly higher permeability in upper regions compared to lower zones. This behavior likely results from gravity-induced blockage of seepage channels by spherical particles, causing a shift from longitudinal to transverse seepage flow. Therefore, engineering assessments of embankment infiltration should emphasize the significance of horizontal permeability.

Navier-Stokes Flow Seepage Simulation

The Stokes flow calculation method in COMSOL was employed to simulate the seepage flow of the REV model at point O of the B-10 model to examine macroscopic seepage characteristics. Fig. 10 reveals that the average flow velocity at the model's outlet increases linearly with the gradual rise of the hydraulic gradient. A comparison of the experimental results from the setup shown in Fig. 9 confirms that the simulation outcomes align with the experimental data. In addition, velocity variations influenced by the initial pressure show differing sensitivities to the hydraulic gradient, with greater sensitivity observed as the free surface is approached.

Although absolute velocity discrepancies between the simulations and experiments exist, potentially due to gradation and scale mismatches, the relative velocity–

Table 2. Comparison of the calculated and tested permeability coefficient of the Loose Gravel Soil.

REV number	Permeability ($10^{-11}m^2$)		Error (%)
	Simulation results	Test results	
A-REV	0.339	0.314	7.96
B-REV	0.341		8.60
C-REV	0.337		7.32
D-REV	0.335		6.69
E-REV	0.33		5.10
F-REV	0.328		4.46
G-REV	0.326		3.82
H-REV	0.329		4.78
O-REV	0.336		7.01

hydraulic gradient relationships at the three pressure depths exhibit consistency with experimental data, affirming the model's reliability.

Connectivity of Pore Structure

The topology of the pore model describes the connectivity relationships between pores and throats. The spatial topology of pore networks is quantitatively characterized through pore coordination number distributions.

REV exhibits comparable throat parameters across spatial positions, where the primary pores show equivalent radii of 0.50-0.61 mm and surface areas between 9-13 mm^2. Distinct maximum coordination numbers are observed across REVs with varying spherical particle contents: B-30 specimens demonstrate peak values of 24, 22, 23, 22, 21, 22, 26, 27, and 28, in contrast to B-10's 30, 27, 29, 30, 28, 29, 27, 30, and 30.

Fig. 11 exhibits that the coordination number distributions of REVs are compared across B-30, B-20, and B-10 configurations at various spatial locations. The results indicate that while spatial heterogeneity exists in coordination number distributions, the cumulative probability curves exhibit similar patterns under constant spherical particle content. For B-30 specimens, 80% of coordination numbers fall within the 3-10 range, while values above 20 constitute less than 2%, indicating attributes of a normal distribution.

A comparison of pore coordination number evolution across B-10, B-20, and B-30 demonstrates that reduced spherical particle content leads to a sequential decrease in REV pore counts (approximately 1900, 1400, and 1000). The modeled coordination number frequency declines progressively, with pores possessing coordination numbers ranging from 1-10 comprising 77%, 82%, and 87% of the total populations. Among these, B-10 exhibits enhanced pore connectivity. The underlying mechanism is attributed to the spatial architecture of spherical particles. Fig. 12 illustrates that higher concentrations of spherical particles increase the likelihood of particle-to-particle interactions. Under identical spatial constraints, the regular geometry of spherical particles results in homogeneous pore structures during packing, characterized by morphological and structural consistency. In contrast, the geometric variability of irregular particles leads

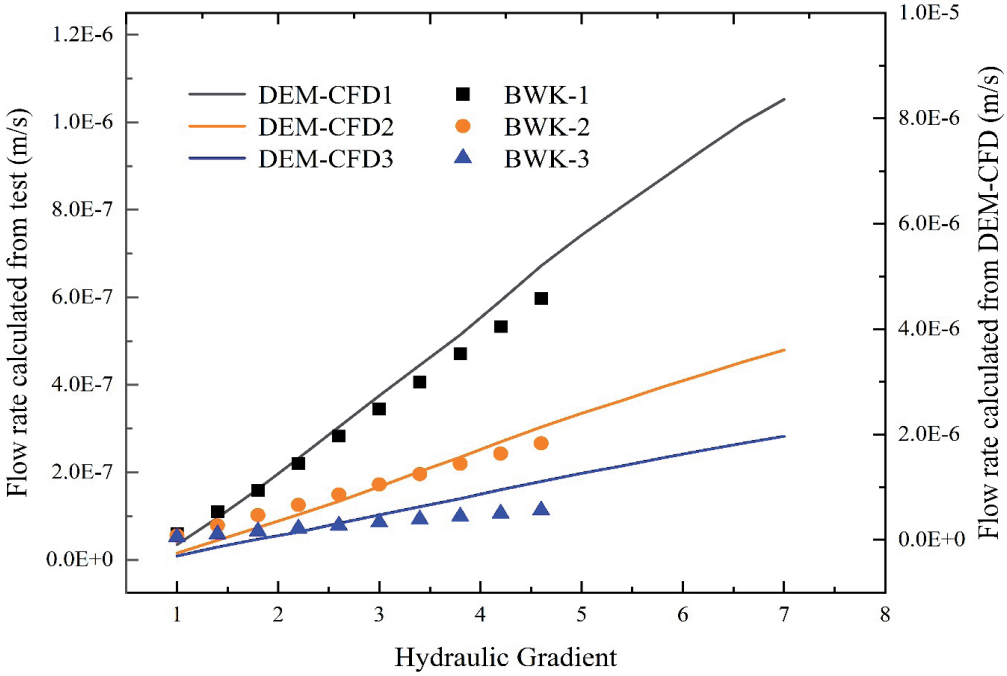

Fig. 10. Comparison of the numerical results and the test results.

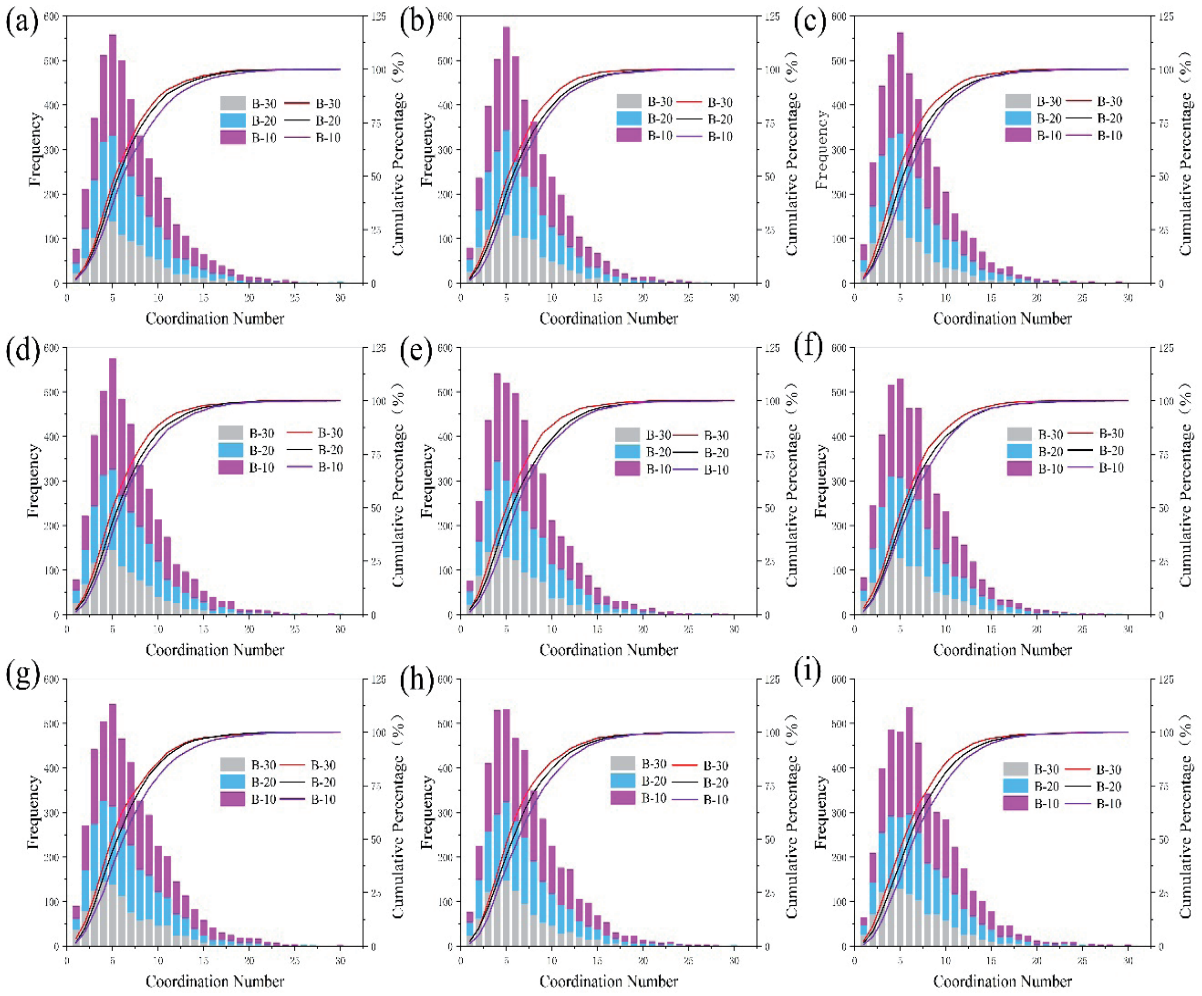

Fig. 11. Coordination number distribution. (a-i) is REV taken at points A, B, C, D, E, F, G, H, and O.

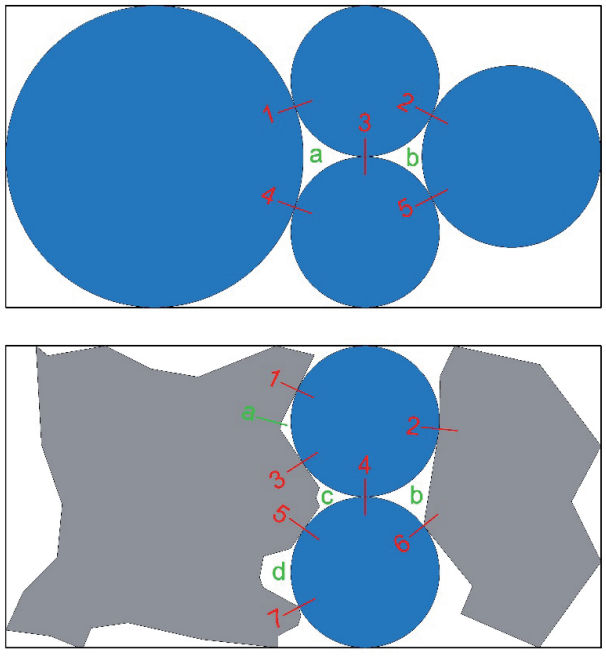

Fig. 12. Comparison of pore structure between real aggregate model and spherical particle model. (1-7) is the contact between particles; (a-d) is the pores between particles.

to complex and disordered pore architectures during packing, where such structural irregularities favor the formation of increased porosity, particularly within the micropore domain.

Pore Diameter Analysis

Pore diameters are obtained by measuring the circumscribed sphere diameters within the three-dimensional reconstructed pore network model. All pore diameters within each REV are statistically analyzed to assess pore size distribution patterns. Fig. 13 presents the frequency distribution histogram of pore diameters.

The frequency curves reveal that pore diameters in B-10, B-20, and B-30 specimens predominantly range from 0.10-1.0 mm, displaying characteristics of a normal distribution. The most frequent pore diameters fall within the 0.26-0.7 mm interval, with mean values ranging from 0.42-0.55 mm and standard deviations between 0.23-0.38.

Current literature classifies pores into four categories based on size: micropores (<10 nm), small pores (10-100 nm), mesopores (100-1000 nm), and macropores (>1000 nm) [61]. Based on this classification, the reconstructed pores in Loose Gravel Soil from this study primarily fall within the macropore range.

Characteristics of Pore Morphology Distribution

Loose Gravel Soil exhibits considerable pore arrangement diversity and randomness due to irregular aggregate particles and an inherently loose structure, with pores displaying highly irregular morphologies [62]. Although simple geometric shapes cannot fully represent pore complexity, shape factors are utilized to quantify irregularity and better approximate actual pore geometries [63]. The formula for calculating the shape factor is provided in Equation (13).

$$C = \frac{VL}{A^2} \tag{13}$$

where V is the pore volume; L is the pore length; A is the pore surface area; C is the pore shape factor.

A larger pore shape factor indicates a more regular pore shape, while a smaller shape factor corresponds to a flatter pore shape. The shape factor of a cube

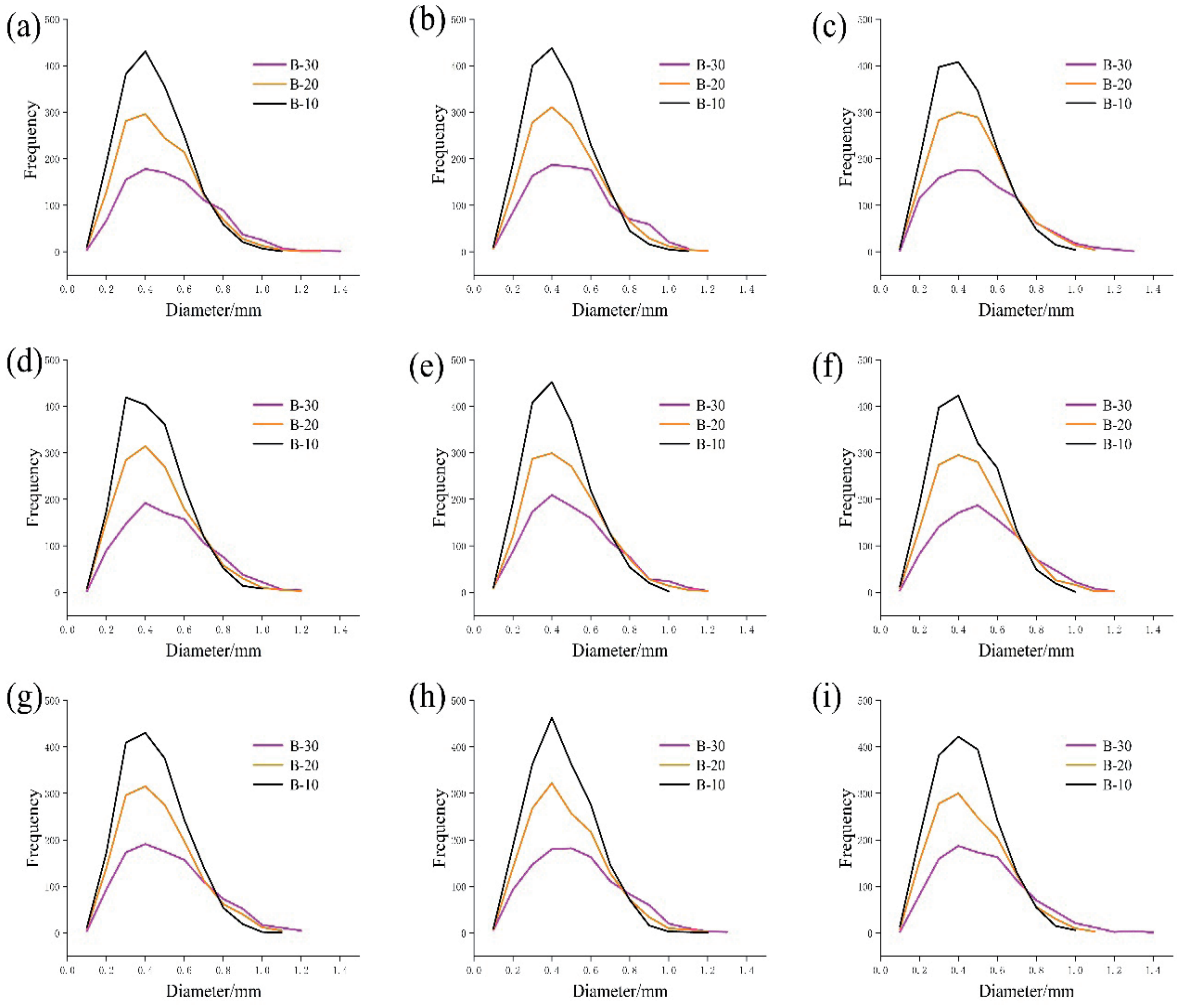

Fig. 13. Distribution curve of pore diameter frequency. (a-i) refers to REV taken at points A, B, C, D, E, F, G, H, O.

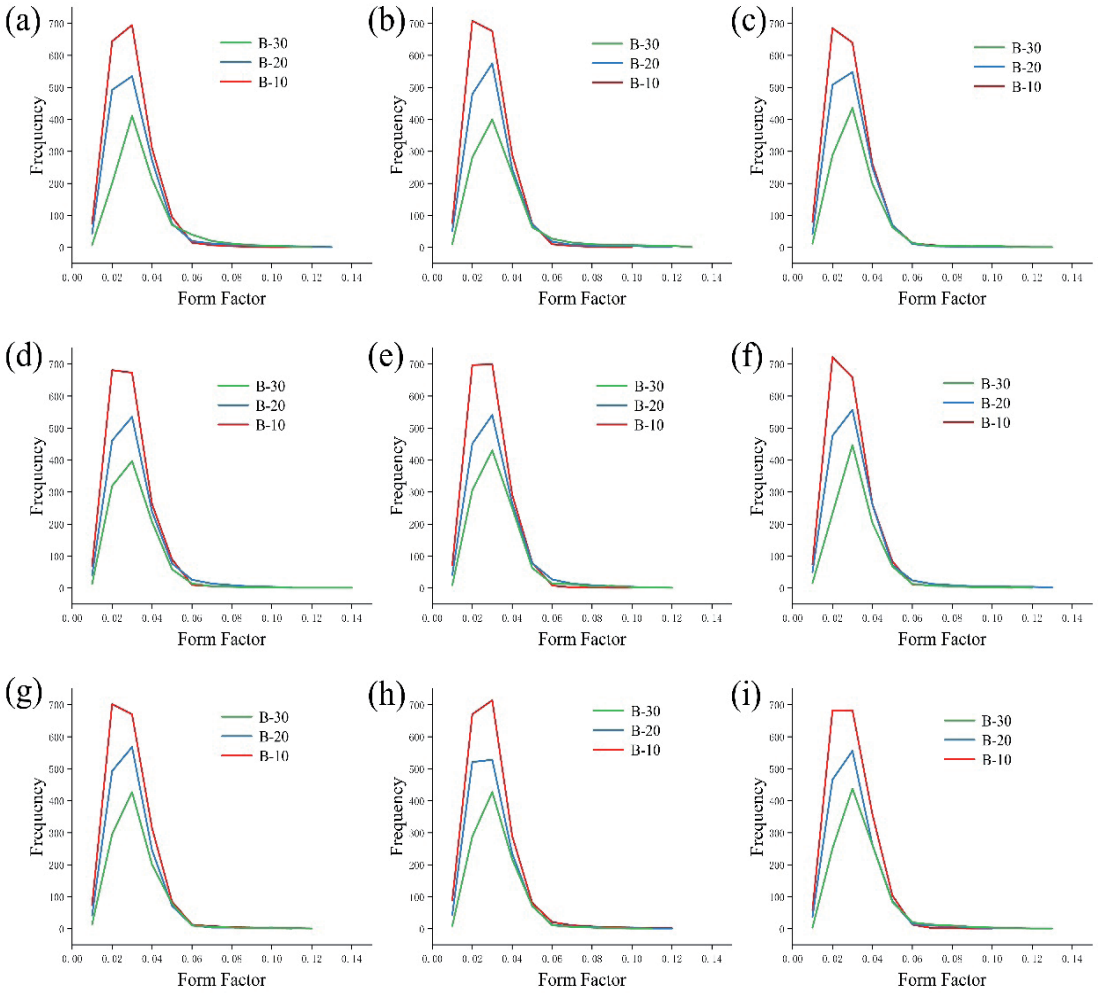

Fig. 14. Distribution curve of pore shape factor frequency. (a-i) is REV taken at points A, B, C, D, E, F, G, H, and O.

is 0.03, that of a sphere is 0.05, and the shape factor of a tetrahedron, which varies in form, ranges from 0 to 0.07.

Using the Label Analysis module in AVIZO software, pore volume, length (derived from circumscribed sphere diameters), and surface area (calculated through voxel quantification) were obtained for each pore. These parameters were then applied in Equation (13) to determine individual pore shape factors. Statistical analysis of shape factors reveals characteristics of pore regularity, as shown in the frequency distribution curves in Fig. 14.

Analysis of shape factor distributions reveals unimodal, near-symmetric patterns across B-10, B-20, and B-30 REVs. Most values fall within the 0.01-0.05 range (normal distribution), with mean values between 0.025-0.035. This indicates that cubic or rectangular prism geometries dominate, while spherical or tetrahedral pores constitute minor components. The structural instability of cubic or rectangular shapes increases their susceptibility to hydraulic-induced damage during seepage flow processes.

Seepage Characteristics

PNM-based seepage flow simulations were conducted for models B-10, B-20, and B-30 in three orthogonal directions (X, Y, Z). Fig. 15 and Fig. 16 illustrate the pressure field configuration and streamline distribution of the velocity field during fluid migration. As the REV pore architecture and connectivity display limited spatial heterogeneity within individual models, the analysis focused solely on REVs located at position O.

Fig. 15 illustrates progressive pressure attenuation along flow paths. Enlarged pore throat dimensions with increased branching are associated with reduced pressure gradients and smoother transitions, whereas geometrically constrained pores retain elevated pressure levels accompanied by intensified pressure oscillations. The pressure field exhibits consistent evolutionary patterns across flow directions, indicating similar behavioral characteristics between transverse and longitudinal flows. The velocity field depicted in Fig. 16 reveals significant flow heterogeneity within the pore structure. Central regions exhibit more continuous and densely clustered streamlines, indicating enhanced

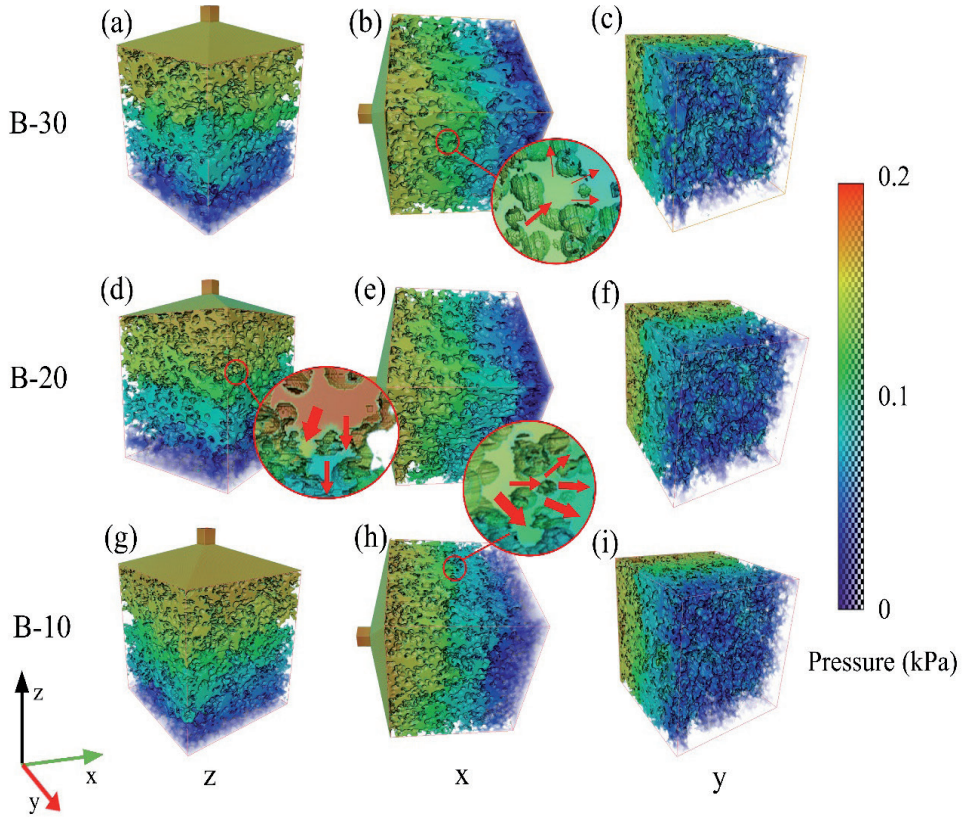

Fig. 15. Pressure field distribution of REVs under different flow directions. (a-c) is the pressure field of REV at point O of B-30 in the X, Y, and Z directions; (d-f) is the pressure field of REV at point O of B-20 in the X, Y, and Z directions; (g-i) is the pressure field of REV at point O of B-10 in the X, Y, and Z directions.

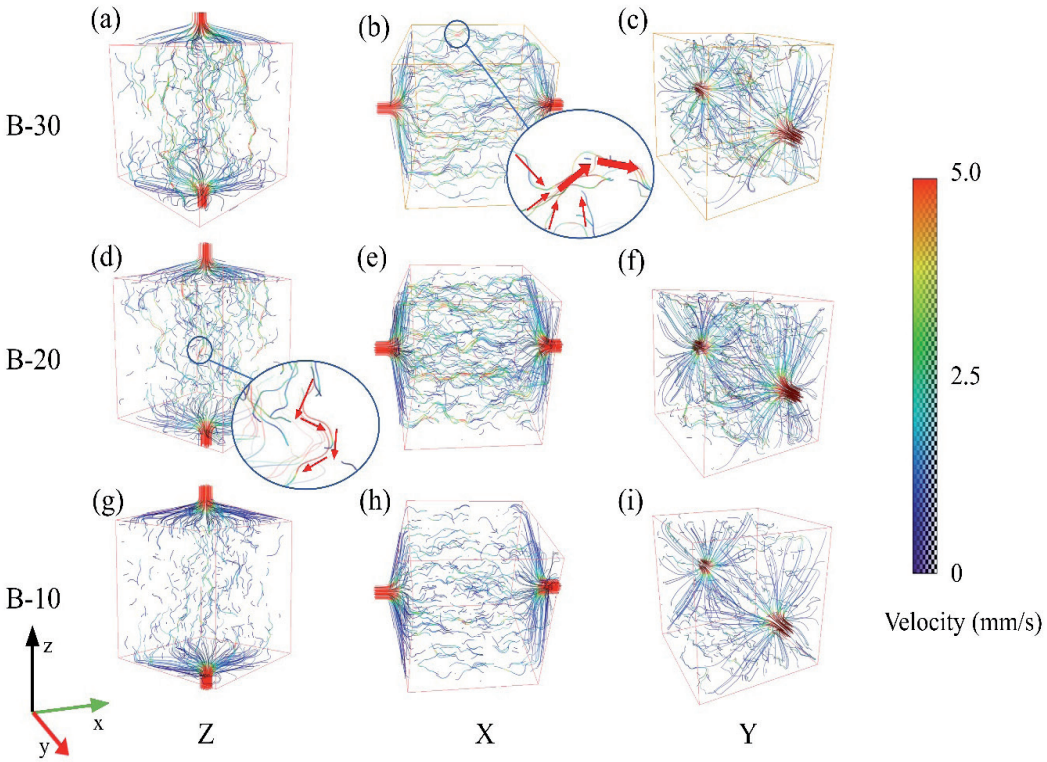

Fig. 16. Velocity field distribution of REV under different flow directions. (a-c) is the flow velocity field of REV at point O of B-30 in the X, Y, and Z directions; (d-f) is the flow velocity field of REV at point O of B-20 in the X, Y, and Z directions; (g-i) is the flow velocity field of REV at point O of B-10 in the X, Y, Z directions.

connectivity. Both X- and Y-direction flows exceed Z-direction flow regarding global connectivity metrics. In addition, across all spherical particle content ratios, REV simulations indicate localized velocity amplifications at throat constrictions, along with concentrated streamline distributions in all flow directions. Increased spherical particle fractions facilitate streamlined flow trajectories with greater stability, improving the global permeability characteristics of the system. In contrast, lower spherical particle concentrations (B-10) produce geometrically complex pore networks due to enhanced aggregate representation, resulting in tortuous flow paths with proliferated micro-channels that substantially reduce permeability efficiency.

Discussion

This study adopts multi-view stereo-matching technology to capture the morphological characteristics of natural aggregate particles in Loose Gravel Soil. DEM data were generated for modeling by analyzing their surface structures. This method facilitates a more accurate representation of the geometric features of aggregate particle surfaces, enabling the simulation of the multi-angular and multifaceted nature of real aggregate structures in the construction of aggregate clusters using PFC 5.0. However, the greater the realism of the aggregate model, the higher the time and computational costs required to simulate the complete virtual sample. Therefore, in constructing the virtual samples, this study employs aggregate cluster modeling for particles larger than d_{10}, d_{20}, and d_{30} in the DEM-CFD gradation curve, while particles below this size range are simplified as spheres. In comparison, Zhang et al. [28] in their virtual modeling of asphalt samples only considered the coarse aggregate portion and excluded the fine particle model. They demonstrated the feasibility of this modeling technique by comparing the hydraulic performance of real and virtual samples.

The following sections will analyze the pore space structures at various locations within the model using fractal theory and the permeability anisotropy index to explore the effect of pore structure heterogeneity, constructed using this modeling approach, on seepage flow behavior.

Fractal Dimension and Heterogeneity of Pore Structure

The fractal dimension serves as a measure of the complexity and dynamic evolution of the internal structure of porous media. The structures of soil, rock, and similar porous materials frequently exhibit distinct fractal characteristics. Among the various methods available for calculating fractal dimensions, the box-counting method is most widely used in geotechnical engineering [64, 65]. This method involves covering the fractal target with small cubes of side length a and counting the number of cubes, N(a), needed to cover the fractal. The fractal dimension D of the porous medium is then calculated using Equation (14). Using AVIZO's 3D fractal module, REV-specific fractal dimensions were obtained, with the B-10 model serving as an example. In this study, AVIZO's 3D fractal module was applied to determine the fractal dimension of the pores at each REV location. For the B-10 model, the fractal dimension was computed to assess the complexity of the pore structure.

$$D = -\frac{\lg N(a)}{\lg a} \tag{14}$$

Table 3 lists the calculated fractal dimensions of the pores. The three-dimensional fractal dimension (D_{3D}) ranges from 2.5882 to 2.6101, indicating minimal overall variation. In contrast, the two-dimensional fractal dimension (D_{2D}) ranges from 1.5147 to 1.6006, with a maximum difference of 0.086. Based on Feng et al. [66], the ideal difference between the three-dimensional and two-dimensional fractal dimensions should be 1.0. In this study, the average difference between the three-dimensional and two-dimensional fractal dimensions is approximately 1.05. This indicates that the pore development and structure are relatively consistent across different REV locations. Although the uneven pore distribution at various locations leads to a slightly greater difference than 1.0, it still conforms to the fractal self-similarity characteristics described by Feng et al.

It is necessary to introduce the concept of pore structure heterogeneity to examine the causes of the non-uniform pore distribution. Previous numerical simulation methods often assume that pore distributions within geotechnical materials are homogeneous, which can result in errors when applied to practical engineering problems. It is essential to fully consider the heterogeneity of pore structures in geotechnical materials to reduce these errors [67].

Table 3. Statistics of fractal dimension.

REV number	D_{3D}	D_{2D}
A-REV	2.6096	1.5469
B-REV	2.6051	1.5238
C-REV	2.5882	1.5605
D-REV	2.6021	1.5404
E-REV	2.5992	1.5147
F-REV	2.5897	1.5412
G-REV	2.6101	1.6006
H-REV	2.6008	1.5706
O-REV	2.5973	1.5515
Mean	2.6002	1.5500

Porosity, pore diameter, and pore shape, as essential parameters characterizing pore structures, can also be utilized to assess pore structure heterogeneity. The heterogeneity coefficient is defined using the coefficient of variation, calculated as the ratio of the standard deviation of the pore structure characterization parameters to their mean values. The magnitude of the heterogeneity coefficient reflects the non-uniformity of these parameters. The primary factors influencing pore structure heterogeneity can be identified by comparing the heterogeneity coefficients.

Fig. 17 shows that the heterogeneity coefficients of the pore structure characterization parameters are compared. Among the three parameters, the heterogeneity coefficient of pore shape is the highest, making it the dominant factor influencing pore structure heterogeneity in this study. In contrast, Wang et al. [61] in their research on coarse-grained sandstone, identified pore diameter as the primary factor affecting pore distribution heterogeneity, followed by porosity, with pore shape exerting a lesser influence. This variation can be related to the porosity of the studied materials. The Loose Gravel Soil structure, compared to sandstone reservoir structures, is more loosely packed and exhibits greater porosity. In addition, the virtual sample generation process leads to more uniform particle deposition than natural conditions, reducing the sensitivity of pore size to spatial structure. As a result, the influence of pore diameter on pore structure heterogeneity is slightly less significant than that of pore shape.

Permeability Anisotropy

The effect of non-uniform pore structure distribution on permeability can be evaluated through permeability anisotropy. The seepage flow behavior of pores at various locations can be analyzed by comparing the permeability ratios in different directions. Typically, the horizontal permeability of a sample exceeds its vertical permeability [68, 69], implying that the anisotropy indices X/Z and Y/Z should be greater than 1. In addition, the greater the deviation of the anisotropy index from 1, the higher the permeability anisotropy.

Table 4 indicates that all anisotropy indices in the REV pore model of B-10 exceed 1. This outcome is attributed to the use of the pre-compaction method, which effectively simulates the deposition of actual samples under natural conditions. During the pre-compaction process, the movement and rotation of aggregate particles result in the displacement of fine particles within the pores, modifying the pore structure. This observation is consistent with the findings of Masad et al. [68] on the anisotropic distribution of permeability in asphalt concrete, indicating that the permeability of Loose Gravel Soil in different directions adheres to objective principles.

In addition, permeability anisotropy does not exhibit a consistent trend across different spatial locations. Several factors, including the non-uniform distribution of particle sizes, the complexity of pore structures, and the irregularity of fractures and bedding, can influence this randomness. The inclusion of additional variables and uncertainties further complicates the prediction and simulation of this randomness.

During actual seepage flow in Loose Gravel Soil bank slopes, the shallow subsurface exhibits permeability anisotropy slightly greater than 1, aligning with the patterns summarized in Table 4 of this study. In deeper slope strata, however, the internal structure of the gravelly sandstone matrix becomes progressively denser due to sedimentation and stacking processes,

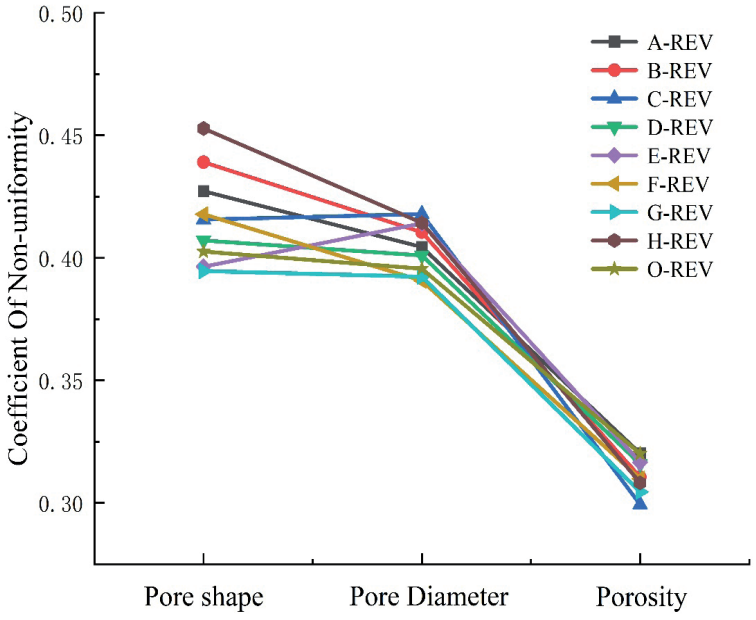

Fig. 17. Comparison of non-uniformity coefficients of pore structure characterization parameters.

Table 4. Comparison of calculated permeability.

REV number	Permeability ($10^{-11}m^2$)			Anisotropy		
	X	Y	Z	X/Y	X/Z	Y/Z
A-REV	0.382	0.475	0.339	0.804	1.127	1.401
B-REV	0.406	0.489	0.341	0.953	1.367	1.434
C-REV	0.380	0.451	0.337	0.858	1.148	1.338
D-REV	0.411	0.514	0.335	0.799	1.227	1.534
E-REV	0.364	0.454	0.33	0.863	1.188	1.376
F-REV	0.372	0.409	0.328	1.020	1.271	1.247
G-REV	0.359	0.484	0.326	0.990	1.469	1.485
H-REV	0.397	0.408	0.329	0.973	1.207	1.240
O-REV	0.432	0.397	0.336	1.098	1.298	1.182
Mean	0.389	0.453	0.333	0.929	1.256	1.360

resulting in lower porosity compared to shallow zones. Concurrently, fine particle migration blocks partial longitudinal seepage paths, weakening vertical seepage behavior (Fig. 18). Driven by hydraulic head differences and porosity gradients, water continuously migrates from high-potential to low-potential zones, redistributing saturation and thereby altering the slope's permeability coefficient and reducing its shear strength. Concurrently, seepage-induced displacements develop within the slope. Although constrained by horizontal permeability, these displacements remain minor. Nevertheless, progressive water infiltration saturates the lower slope strata, increasing pore water pressure and diminishing slope strength. As the soil's mechanical properties degrade, the upper slope becomes susceptible to sliding failure under gravitational loading.

The preceding discussion demonstrates the validity of the proposed modeling method from the perspectives of fractal dimension and permeability anisotropy. Compared to traditional DEM spherical modeling and nondestructive electronic detection techniques for extracting pore structures, the approach of scanning and modeling actual aggregate particles employed in this study better simulates the real structural state of geotechnical materials. In addition, extracting pore structures using this method is more convenient than techniques such as CT scanning. The pore structure can be altered, resulting in more accurate outcomes in seepage flow simulations by adjusting the DEM particle gradation and the precision of aggregate modeling. This provides a practical and effective methodology and framework for future investigations into microscopic pore-scale seepage flow problems, such as reservoir slope instability. However, during the accumulation of Loose Gravel Soil, aggregate particles form a specific inclination angle with the ground due to gravitational forces. Variations in this inclination angle inevitably affect the stability of slope seepage flow to varying

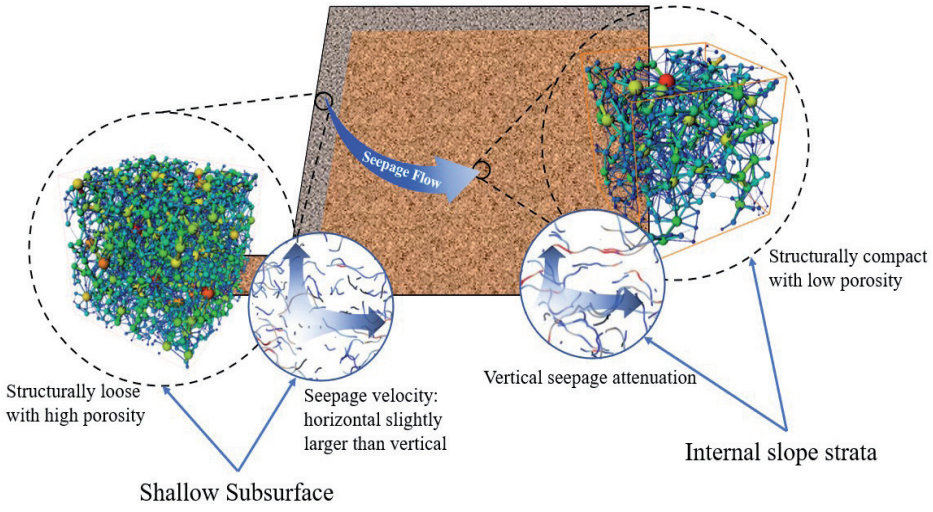

Fig. 18. Influence of bank slope pore structure on seepage flow behavior.

extents [70], a factor not yet considered in this study. Therefore, it is recommended that future applications of the proposed modeling method incorporate the effects of aggregate particle inclination to more accurately simulate seepage flow conditions in slopes under different accumulation processes. In addition, the primary causes of engineering problems, such as dam breaches and slope instability following reservoir impoundment, are the heterogeneity of internal pore spaces and internal erosion caused by the migration of fine particles [25]. This study currently focuses on single-phase flow in seepage flow paths and does not thoroughly examine internal erosion. Investigating fluid-solid coupling issues from the perspective of microscopic pores using the DEM-CFD method is a critical direction for future engineering research. Therefore, future studies on pore-scale seepage flow should highlight the influence of internal erosion. In addition, to address the computational challenges associated with DEM, machine learning and deep learning techniques can be integrated to predict and monitor internal erosion [24], enabling early identification of potential risks in geotechnical slopes and reservoir dams and supporting timely preventive actions.

Conclusions

This study proposes a novel 3D pore reconstruction methodology for Loose Gravel Soil from the Yellow River stone forest, employing Representative Elementary Volume (REV) analysis to investigate pore structures and seepage flow characteristics. The key conclusions are as follows:

(1) Multi-view stereoscopic modeling facilitates DEM construction for individual aggregate particles, accurately replicating natural pore configurations while providing operational flexibility, cost efficiency, and reduced hardware requirements. The editable nature of each generated model supports 3D pore network reconstruction in heterogeneous soil–rock composites.

(2) REV dimension optimization using nine-point sampling identified 540 voxels (8.64×8.64×8.64 mm^3 cube) as the representative scale for Loose Gravel Soil pore networks. Reductions in spherical particle fractions lead to lower permeability estimation errors, with B-10/B-20/B-30 REVs showing maximum deviations ranging from 8.6% to 27.7%, validating the model's rationality. Agreement between Stokes flow predictions and experimental velocity profiles confirms simulation accuracy, establishing the framework's capability for seepage flow modeling.

(3) REV analysis shows that pore coordination numbers predominantly fall below 20 with consistent distribution trends. Models containing fewer spherical particles exhibit higher maximum coordination numbers and enhanced pore connectivity, thus impeding the formation of preferential flow channels during seepage. Pore space analysis of Loose Gravel Soil reveals a normal distribution of pore diameters, with a prevalence of unstable cubic and rectangular configurations. Spherical and tetrahedral pores account for a minor proportion. Comparative fractal dimension analysis indicates similar pore development patterns and structural homogeneity across spatial locations, making the pore architecture more vulnerable to failure induced by seepage flow. Heterogeneity analysis of porosity, pore diameter, and pore morphology identifies pore geometry as the primary factor influencing structural heterogeneity.

(4) PNM flow simulations demonstrate permeability anisotropy indices greater than 1, with higher connectivity during lateral flow compared to longitudinal flow. This indicates that Loose Gravel Soil exhibits greater horizontal than vertical permeability, implying accelerated lateral infiltration and erosion of bank slopes following reservoir impoundment. Simultaneously, intra-pore pressure declines progressively along flow paths, with throat dimensions and branching frequency significantly affecting pressure gradients. Sharp velocity fluctuations occur at pore constrictions and throat transitions. These zones of intense hydrodynamic variation serve as key initiation sites for failure during embankment seepage.

Acknowledgments

This work was supported by the National Natural Science Foundation of China (Grant No. 42167043 and 51269009), Gansu Provincial Key Research and Development Program, China (20YF8ND141). The authors would like to thank MogoEdit (https://www.mogoedit.com) for its English editing during the preparation of this manuscript.

Conflict of Interest

The authors declare no conflict of interest.

References

1. RINALDI M., CASAGLI N. Stability of streambanks formed in partially saturated soils and effects of negative pore water pressures: the Sieve River (Italy). Geomorphology. **26** (4), 253, **1999**.
2. SIMA L., WANG C., WANG L., WU F., MA L., WANG Z. Effect of pore structure on the seepage characteristics of tight sandstone reservoirs: A case study of Upper Jurassic Penglaizhen Fm reservoirs in the western Sichuan Basin. Natural Gas Industry B. **4** (1), 17, **2017**.
3. GAO M., GAO Z., YANG B.G., XIE J., WANG M.Y., HAO H.C., WANG J.Y. Macroscopic and microscopic mechanical behavior and seepage characteristics of coal under hydro-mechanical coupling. Journal of Central South University. **31** (8), 2765, **2024**.
4. LI B.G., ZHANG H., WANG G., LIU G., GAO W.D., ZHU K., CHEN C. Explore the "Transparent" Soils:

Soilporelogy Has Sailed. Acta Pedologica Sinica. **60** (5), 1221, **2023** [In Chinese].
5. SHEN H., BI J.F., LUO X.Q. Numerical simulation of internal erosion characteristics of block in matrix soil aggregate. Rock and Soil Mechanics. **38** (5), 1497, **2017** [In Chinese].
6. HOU T.S., XU G.L., ZHANG D.Q., LIU H.Y. Stability analysis of Gongjiacun landslide in the three Gorges Reservoir area under the action of reservoir water level fluctuation and rainfall. Natural Hazards. **114** (2), 1647, **2022**.
7. ZHANG Y., ZHANG Z., XUE S., WANG R., XIAO M. Stability analysis of a typical landslide mass in the Three Gorges Reservoir under varying reservoir water levels. Environmental Earth Sciences. **79**, 1, **2020**.
8. SUN L., WANG X.Q., JIN X., LI J.M., WU S.T. Three dimensional characterization and quantitative connectivity analysis of micro/nano pore space. Petroleum Exploration and Development. **43** (3), 490, **2016** [In Chinese].
9. MO B., GUO Z., LI Y., ZHU D., ZENG X.J., LI X.Y., WU Y. In situ investigation of the valence states of iron-bearing phases in Chang'E-5 lunar soil using FIB, AES, and TEM-EELS techniques. Atomic Spectroscopy. **43**, 53, **2022**.
10. SONG Y., DAI G., ZHOU J., BIAN Z., ZHAO L., SONG L. Characterizing porous volume of cement-based concrete by multiscale image analysis. Journal of Materials in Civil Engineering. **32** (9), 04020267, **2020**.
11. YU B., DIJKSTRA T.A., FAN W., SMALLEY I.J., WEI Y.N., DENG L.S. Advanced multi-scale characterization of loess microstructure: Integrating μXCT and FIB-SEM for detailed fabric analysis and geotechnical implications. Engineering Geology. **341**, 107727, **2024**.
12. KUANG X., SANSALONE J., YING G., RANIERI V. Pore-structure models of hydraulic conductivity for permeable pavement. Journal of Hydrology. **399** (3-4), 148, **2011**.
13. GRUBEŠA I.N., BARIŠIĆ I., DUCMAN V., KORAT L. Draining capability of single-sized pervious concrete. Construction and Building Materials. **169**, 252, **2018**.
14. LIU J., SONG R. Investigation of water and CO_2 flooding using pore-scale reconstructed model based on micro-CT images of Berea sandstone core. Progress in Computational Fluid Dynamics, An International Journal. **15** (5), 317, **2015**.
15. LAMANDÉ M., SCHJØNNING P., DAL FERRO N., MORARI F. Soil pore system evaluated from gas measurements and CT images: A conceptual study using artificial, natural and 3D-printed soil cores. European Journal of Soil Science. **72** (2), 769, **2021**.
16. APELEO ZUBIRI B., WIRTH J., DROBEK D., ENGLISCH S., PRZYBILLA T., WEISSENBERGER T., SPIECKER E. Correlative Laboratory Nano-CT and 360 Electron Tomography of Macropore Structures in Hierarchical Zeolites. Advanced Materials Interfaces. **8** (4), 2001154, **2021**.
17. WANG M. Resistivity numerical simulation and its influence law analysis based on multi-component 3D digital core of glutenite. Petroleum Geology and Recovery Efficiency. **31** (6), 33, **2024** [In Chinese].
18. AKAND L., YANG M., GAO Z. Characterization of pervious concrete through image based micromechanical modeling. Construction and Building Materials. **114**, 547, **2016**.
19. GARCIA DIEZ J.L., GONZALEZ GALINDO J., SORIANO PEÑA A., Universidad Politécnica de Madrid. Adjustment of a numerical model for pore pressure generation during an earthquake. Plos One. **14** (9), e0222834, **2019**.
20. CAI J., QIN X., XIA X., JIAO X., CHEN H., WANG H., XIA Y. Numerical modeling of multiphase flow in porous media considering micro-and nanoscale effects: A comprehensive review. Gas Science and Engineering. 205441, **2024**.
21. TAHMASEBI P., JAVADPOUR F., SAHIMI M. Stochastic shale permeability matching: Three-dimensional characterization and modeling. International Journal of Coal Geology. **165**, 231, **2016**.
22. LU Y., LIU Z.B., LIAO X.W., LI C., LI Y. Automatic classification of pore structures of low-permeability sandstones based on self-organizing-map neural network algorithm. Bulletin of Geological Science and Technology. **43** (6), 318, **2024** [In Chinese].
23. BAMMOU Y., BENZOUGAGH B., ABDESSALAM O., BRAHIM I., KADER S., SPALEVIC V., ERCISLI S. Machine learning models for gully erosion susceptibility assessment in the Tensift catchment, Haouz plain, Morocco for sustainable development. Journal of African Earth Sciences. **213**, 105229, **2024**.
24. VAN PHONG T., TRINH P.T., THANH B.N., VAN HIEP L., PHAM B.T. Comparative analysis of machine learning and deep learning methods for coastal erosion susceptibility mapping. Earth Science Informatics. **18** (1), 92, **2025**.
25. XIONG H., ZHANG Z., BAO X., WU H., YIN Z.Y., CHEN X. Micro-mechanical analysis of particle shape effect on suffusion of gap-graded soils. Computers and Geotechnics. **165**, 105925, **2024**.
26. ZOU Y., CHEN C., ZHANG L. Simulating progression of internal erosion in gap-graded sandy gravels using coupled CFD-DEM. International Journal of Geomechanics. **20** (1), 04019135, **2020**.
27. ZHANG J., XIA S., HU N., HAO W., HAN R., MENG B., ZHANG Z. Optimization of anti-clogging pervious pavement structure based on numerical evaluation. Construction and Building Materials. **275**, 122186, **2021**.
28. ZHANG Z., QIAO Y., GIUSTOZZI F. Modelling the hydraulic performance of open graded asphalt using the discrete element method and computational fluid dynamics. Journal of Hydrology. **621**, 129612, **2023**.
29. PIERALISI R., CAVALARO S.H.P., AGUADO A. Advanced numerical assessment of the permeability of pervious concrete. Cement and Concrete Research. **102**, 149, **2017**.
30. GE Y., ZHOU A., NAZEM M., DENG Y. Numerical simulation of cone penetration test by using CFD–DEM coupled analysis. Acta Geotechnica. **19** (11), 7635, **2024**.
31. WEBB W., TURNBULL B., LEONARDI A. Performance and limits of a geotechnical centrifuge: DEM-LBM simulations of saturated granular column collapse. Granular Matter. **26** (2), 32, **2024**.
32. KOESTEL J., LARSBO M., JARVIS N. Scale and REV analyses for porosity and pore connectivity measures in undisturbed soil. Geoderma. **366**, 114206, **2020**.
33. CAI P., MAO X., HE P., LAI X. Quantifying Three-Dimensional Macropore Structure and Seepage Characteristics of Representative Elementary Volume for Recycled Aggregate Pervious Concrete. Journal of Materials in Civil Engineering. **36** (5), 04024092, **2024**.
34. SUN X., TAKAHASHI K., SHIMOMURA Y., TAKIZAWA H., WANG X. Performance evaluation of the LBM simulations in fluid dynamics on SX-

Aurora TSUBASA vector engine. Computer Physics Communications. **307**, 109411, **2025**.
35. SATO K., KAWASAKI K., KOSHIMURA S. A comparative study of the cumulant lattice Boltzmann method in a single-phase free-surface model of violent flows. Computers & Fluids. **236**, 105303, **2022**.
36. ZHANG J., MA G., YANG Z., MA Q., ZHANG W., ZHOU W. Investigation of flow characteristics of landslide materials through pore space topology and complex network analysis. Water Resources Research. **58** (9), e2021WR031735, **2022**.
37. SHIRE T., O'SULLIVAN C., HANLEY K.J., FANNIN R.J. Fabric and effective stress distribution in internally unstable soils. Journal of Geotechnical and Geoenvironmental Engineering. **140** (12), 04014072, **2014**.
38. WANG X., HUANG B., TANG Y., HU T., LING D. Microscopic mechanism and analytical modeling of seepage-induced erosion in bimodal soils. Computers and Geotechnics. **141**, 104527, **2022**.
39. GUO W.L., ZHU J.G., WEN Y.F. Unified description for four grading scale methods for coarse aggregate. Chinese Journal of Geotechnical Engineering. **140** (12), 04014072, **2014** [In Chinese].
40. XIE D.S., CAI H., WEI Y.Q., LI W.C. Scaling principle and method in seepage tests on coarse materials. Chinese Journal of Geotechnical Engineering. **37** (2), 369, **2015** [In Chinese].
41. CHU D., WANG L., LI J., LI Z., HUANG J., LI S. Research on ground point cloud filtering method based on WPA-CSF. Progress in Geophysics. **38** (5), 1919, **2023** [In Chinese].
42. LI L., WANG J., YANG S., KLEIN B. A voxel-based clump generation method used for DEM simulations. Granular Matter. **24** (3), 89, **2022**.
43. TAGHAVI R. Automatic clump generation based on mid-surface. In Proceedings, 2nd international FLAC/DEM symposium, Melbourne. pp. 791, **2011**.
44. LEI H.Y., WANG T.Y., ZHANG Z.P., LU H.B., LIU M. Macro-and meso-analysis of newly formed highly viscous dredger fill under vacuum preloading using particle flow theory. Journal of Jilin University (Earth Science Edition). **47** (6), 1784, **2017**.
45. JIA W.L., CHANG C.Y, LI P.R., ZHANG Z.W., XU J.H., YANG J.Y. Numerical simulation of earthquake-induced loess landslides based on particle flow method. Acta Seismologica Sinica. **44** (4), 677, **2022** [In Chinese].
46. WANG J., ZHUANG J.Q., KONG J.X., MOU J.Q., ZHENG J., FU Y.T. Influence of fragmentation on dynamic characteristics of loess landslide based on DEM simulation. Journal of Engineering Geology, **31** (2), 502, **2023** [In Chinese].
47. LI Y., WEI Z.W., LIU C.K., YUAN M.N., WANG J. Application of serial sectioning technology in three-dimensional reconstruction. Ordnance Material Science and Engineering. **42** (1), 127, **2019** [In Chinese].
48. LIU X., XIONG J., LIANG L.X., YUAN W. Study on the characteristics of pore structure of tight sand based on micro-CT scanning and its influence on fluid flow. Progress in Geophysics. **32** (3), 1019, **2017**.
49. FANG H.H., SANG S.X., LIU S.Q., WANG H., ZANG L.Y. Study of digital petrophysical analysis method based on micro-focus X-ray tomography: a case study from No. 3 coal seam of Bofang mining area in southern Qinshui basin. Coal Geology & Exploration. **46** (5), 167, **2018**.
50. CALLOW B., FALCON-SUAREZ I., MARIN-MORENO H., BULL J.M., AHMED S. Optimal X-ray micro-CT image based methods for porosity and permeability quantification in heterogeneous sandstones. Geophysical Journal International. **223** (2), 1210, **2020**.
51. FERNANDES J.S., APPOLONI C.R., FERNANDES C.P. Determination of the representative elementary volume for the study of sandstones and siltstones by X-ray microtomography. Materials Research. **15**, 662, **2012**.
52. WU H., ZHOU Y., YAO Y., WU K. Imaged based fractal characterization of micro-fracture structure in coal. Fuel. **239**, 53, **2019**.
53. CHU Z.X., ZHOU G.Q., RAO Z.H., ZHAO S.G., SHANG X.Y., LI R.L. Porosity-based representative elementary volume for geomaterials and its fractal theory based approximate criterion. Scientia Sinica Technologica. **51** (9), 1107, **2021** [In Chinese].
54. MIN K.B., JING L. Numerical determination of the equivalent elastic compliance tensor for fractured rock masses using the distinct element method. International Journal of Rock Mechanics and Mining Sciences. **40** (6), 795, **2003**.
55. HASSANABADI M., AKHTAR S., AUNE R.E. Study and Modelling of Fluid Flow in Ceramic Foam Filters. Materials. **16** (17), 5954, **2023**.
56. ZHANG P., MU L., HUANG M. A coupled CFD-DEM investigation into hydro-mechanical behaviour of gap-graded soil experiencing seepage erosion considering cyclic hydraulic loading. Journal of Hydrology. **624**, 129908, **2023**.
57. MU L., ZHANG P., SHI Z., HUANG M. Coupled CFD-DEM investigation of erosion accompanied by clogging mechanism under different hydraulic gradients. Computers and Geotechnics. **153**, 105058, **2023**.
58. ZHAO J., HE X., LAI Q., YU B., WU Z. Model of permeability prediction for carbonate rocks based on digital cores. Progress in Geophysics. **39** (6), 2207, **2024** [In Chinese].
59. MENG Y.Q., JIANG J.G., WU J.C. Predicting permeability of porous media from pore structure features of slices by machine learning. Geological Journal of China Universities. **30** (1), **2024** [In Chinese].
60. SONG Y.J., ZHOU Y.T., TANG X.M., WANG Y.L., ZHANG H., CHEN L. Method for determination of permeability of shaly sand formation with low porosity and permeability based on efficient flow pore. Progress in Geophysics. **31** (1), 327, **2016** [In Chinese].
61. WANG S., XU Y., ZHANG Y.B., YAO X.L., WANG L. Microscopic experimental study on the heterogeneity and quantitative characterization of mineral grains and pore structures in coarse-grained glutenites. Journal of China Coal Society. **49** (S2), 832, **2024** [In Chinese].
62. GAO Y., RAEINI A.Q., BLUNT M.J., BIJELJIC B. Dynamic fluid configurations in steady-state two-phase flow in bentheimer sandstone. Physical Review E. **103** (1), 013110, **2021**.
63. MASON G., MORROW N.R. Capillary behavior of a perfectly wetting liquid in irregular triangular tubes. Journal of Colloid and Interface Science. **141** (1), 262, **1991**.
64. FOROUTAN-POUR K., DUTILLEUL P., SMITH D.L. Advances in the implementation of the box-counting method of fractal dimension estimation. Applied Mathematics and Computation. **105** (2-3), 195, **1999**.
65. XUE S., JIANG X.S., DUAN J.M. An improved box-counting method for calculating image fractal dimension. Journal of University of Science and Technology of China. **48** (6), 504, **2018** [In Chinese].

66. FENG Y., YU B., ZOU M., XU P. A generalized model for the effective thermal conductivity of unsaturated porous media based on self-similarity. Journal of Porous Media. **10** (6), **2007**.
67. TANG C.A., KAISER P.K. Numerical simulation of cumulative damage and seismic energy release during brittle rock failure-part I: fundamentals. International Journal of Rock Mechanics and Mining Sciences. **35** (2), 113, **1998**.
68. MASAD E., OMARI A.A., CHEN H.C. Computations of permeability tensor coefficients and anisotropy of asphalt concrete based on microstructure simulation of fluid flow. Computational Materials Science. **40** (4), 449, **2007**.
69. GAXIOLA-HERNÁNDEZ A., OSSA-LÓPEZ A., ALMARAL-SÁNCHEZ J.L., LLANES-CÁRDENAS O. Laboratory determination of hydraulic anisotropy of dense graded asphalt concrete. Ingeniería e Investigación. **38** (1), 67, **2018**.
70. JIANG H.Y., WANG S.N., GAO X.Q., WU Z.J., LI M.W., GU L.L. Permeability characteristics and empirical prediction of cementitious soil rock mixtures based on numerical experiments of mesostructure. Computers and Geotechnics. **177**, 106813, **2025**.